Design of An Electromagnetic Energy Harvesting System Applied to The Shock Absorber of A Sport Utility Vehicle: Part I. Single Permanent Magnet Layer Coreless Type

Minh-Trung Duong[1,2], Yon-Do Chun[1,2]*, Pil-Wan Han[2], Byoung-Gun Park[1,2], Deok-Je Bang[2], and Jin-Kyu Lee[1,2]

[1]*University of Science and Technology, Yuseong-gu, Daejeon 34113, Korea*
[2]*Korea Electrotechnology Research Institute, Seongsan-gu, Changwon 51543, Korea*

This paper deals with the design of an electromagnetic energy harvesting generator for the suspension system of a sport utility vehicle. The proposed generator is composed of a single coreless type permanent magnet layer, which increases flux density across the coil windings and eliminates flux leakage by using the Halbach PM array, thus improving the machine's performance, including flux linkage and output power. The goal of the system is to regenerate energy from the kinetic energy of the suspension system of the sport utility vehicle. The proposed generator physically combines electrical and mechanical components, in which permanent magnets, coil windings, and back iron are attached to the body of the shock absorber. The design's performance was investigated using the finite element method (FEM) and validated by comparison with experimental data.

Keywords : electromagnetic energy harvesting, tubular machine, Halbach array, shock absorber

1. Introduction

Methods of harvesting energy from a vehicle suspension system have been widely studied and developed, especially the tubular linear permanent magnet generator. For a mid-size passenger car on an average road travelling at 60 mph, the average harvestable energy is estimated to range from 100-400 watts [10-12]. If this otherwise dissipated energy can be regenerated, the fuel efficiency of conventional vehicles can be increased by 2% to 9%.

Zuo *et al.* [10] proposed a technique using a tubular generator for harvesting kinetic energy from a vehicle's shock absorber, with the goal of replacing the traditional mechanical suspension system. The electromagnetic suspension system, generated about 16 W to 64 W in a medium size car when moving at a speed of 60 mph on a class C road. In order to increase the performance, X. Tang *et al.* [11] modified a single PM layer model in [10] to be double PM layers, and optimized the output power and power density. This modification led to increases in power density of 5 times, and power generation of 8 times.

Using the configuration reported in [11], which proposed a device combining a mechanical damping part and electrical components, the design in [12] was composed of double permanent magnet (PM) layers attached to a damping body part. The other winding layer was wound around and attached to the back iron frame. Although the volume of the generator was increased, the electrical airgap is significantly larger than the one in [10], and therefore, this model only produced 98.3 W under the same conditions.

The main advantages of the linear electromagnetic shock absorber are high energy conversion efficiency, and design simplicity in comparison with a rotating harvester [6]. However, one of its most significant shortcomings is limited power density.

In most conventional studies on energy harvesting with a vehicle suspension system, the traditional shock absorber is generally replaced by an electromagnetic shock absorber, which is complex and significantly difficult to control to ensure road handling and ride comfort [9-11]. Another study in [13] proposed an active electromagnetic suspension system, which combined a brushless tubular permanent-

*Corresponding author: Tel: +82-55-280-1427
Fax: +82-55-280-1490, e-mail: ydchun@keri.re.kr

magnet actuator with a passive spring. However, the design in [13] was applied to an active suspension system, which requires input power to operate.

Unlike the previous studies mentioned above, this paper focuses on the design and verification of a semi-active suspension system, a combination of a coreless tubular permanent-magnet generator and a conventional hydraulic shock absorber. This topology can potentially harvest dissipated power when a car is moving on an uneven road without any absorbed power. The proposed system was based on the actual dimensions of a commercial shock absorber in an SUV car, and on the available space envelope in a Korando car – an SUV model. The remaining design parameters are presented in detail in the next section. The primary electrical components are schematically depicted, including an inner PM ring, which is attached to the body of the damping part, while a coil winding layer is wound around the PM ring and attached to a back iron.

By using a Halbach array for the PMs arrangement, flux linkage across the coil windings is increased while flux leakage is eliminated. Protecting the system from dust and other environmental risks was not considered in [10]. In this paper, the PM layer in the proposed topology was wrapped with a stainless steel cover, which leads to an increase in the electrical airgap.

Finally, an analysis was carried out using extensive 2D FEM, and the system performance was validated by comparing the simulation with results from corresponding experiments using a fabricated prototype.

2. Design Concepts and Specifications

2.1. Design concepts

Figure 1 shows the cross section of the original shock absorber in an SUV-Korando car and after its modification with the additional electrical components for a single layer PM coreless model. The overlapping length of the magnet array and coil windings is about 200 mm, but fortunately, it is adjustable by ± 40 mm. That is also the same condition for the outer diameter, which can be flexibly chosen from 80 mm to 160 mm, while the inner diameter has to be at least 40 mm, the same as the diameter of the damping part or mechanical part. A half cross-section of the proposed generator is presented in Fig. 2.

Based on the optimized designs in [11], the PMs are arranged using a Halbach array. In this study, the coil windings are supported by an insulation layer instead of iron material, and the PMs are wrapped with a stainless steel layer to prevent from dust and mechanical damage.
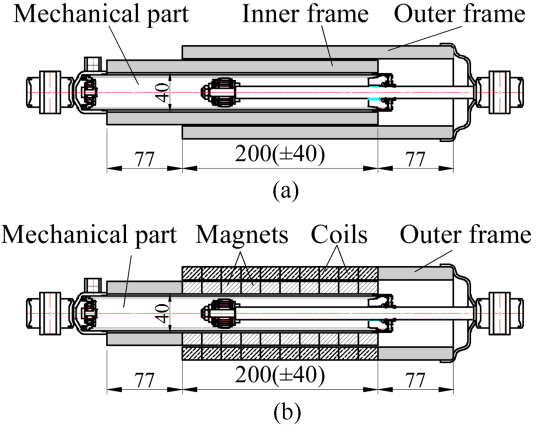

Fig. 1. (Color online) (a) Actual dimensions of a shock absorber; (b) additional electrical components.
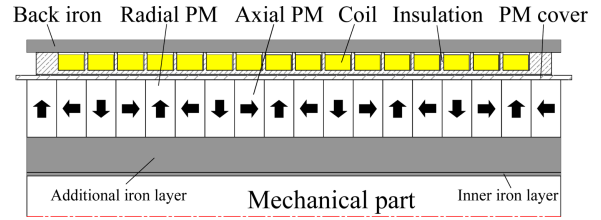

Fig. 2. (Color online) Half cross-section of the single PM layer coreless model.

Ideally, the ratio between the number of poles and the number of slots is $N_p : N_s = 8 : 16$, nevertheless, 9 poles was chosen in this study to avoid the end effect.

The induced electromotive force or coil voltage V_e produced by coil movement with speed v_z (m/s) within the magnetic field B_r (T) is obtained by integrating the Lorentz field $E_{Lorentz}$ over the coil winding length [9]:

$$V_e = \int_0^L E_{Lorentz} dL \approx B_r v_z L \tag{1}$$

where L is the coil winding length.

The maximum current generated by the device with a short circuit is given by the equation:

$$I_0 \approx \sigma B_r v_z A_w \tag{2}$$

where σ ($\Omega \cdot m^{-1}$) is the wire electrical conductivity and A_w is the cross-sectional area of the coil winding wire.

The maximum open circuit voltage V_e and short circuit current I_0 occur at the maximum displacement velocity v_{max}. The maximum instantaneous coil power occurs for a matched load at the maximum displacement velocity v_{max} when the load resistance R_L is equal to the sum of the coil resistance R_c [10]:

$$P_{max} = V_e I_0 = B_r^2 v_z^2 \sigma V_{coil} \tag{3}$$

where $V_{coil}=LA_w$ is the coil volume.

Eq. (3) shows that output power is proportional to the square of the flux density, and the square of the vibrating speed and volume of the coil. Because of the reciprocating movement, the vibrating speed is [10]:

$$v_z(t) = v_{max}\sin \omega t \qquad (4)$$

and the coil position $z(t)$ can be calculated as:

$$z(t) = z_0 - (v_{max}/\omega)\cos \omega t \qquad (5)$$

where z_0 is the initial position of the coil.

From Eq. (5), the relation between half stroke, vibrating frequency and speed can be determined:

$$Stroke_{half} = \frac{v_{max}}{\omega} = \frac{v_{rms}\sqrt{2}}{2\pi f} \qquad (6)$$

2.2. Design specifications

Similar to the design in [9, 10], there are four coil sets over one cycle of the PMs excited flux density. Due to the relative positions between each coil phase with the excited flux density from the PMs, there are differences in the power distribution on each coil phase.

Figure 3 and Fig. 4 show the relative position between the coil phases and flux density over one cycle in an ideal case. To reduce the complexity of the electronics drive in the external circuit, phase 1 is in the series connection of coil 1 and coil 3, while phase 2 is in the series connection of coil 2 and coil 4.
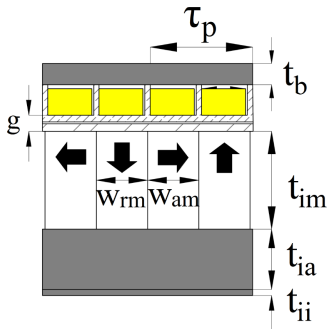

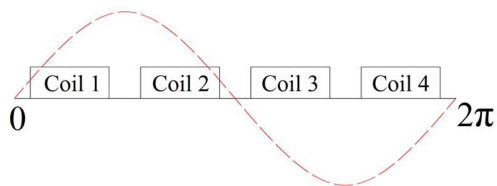**Fig. 3.** (Color online) Configuration of one coil set.

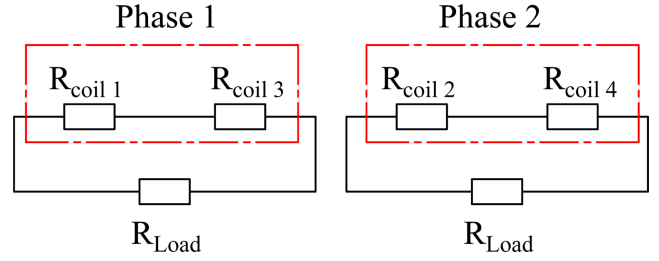**Fig. 4.** (Color online) Relative position between the coil phases and flux distribution.

Fig. 5. (Color online) External circuit connection.

Table 1. Design specifications of the two studied models.

Item	Value
Length, L (mm)	243
Outer diameter, D (mm)	160
PM thickness, t_{im} (mm)	26.0
Radial PM width, w_{rm} (mm)	13.5
Axial PM width, w_{am} (mm)	13.5
Pole pitch, τ_p (mm)	27.0
Coil window thickness, t_c (mm)	8.0
Coil window width, w_c (mm)	12.1
Electrical air gap, g (mm)	4.3
Inner iron thickness, t_{ii} (mm)	1.6
Added iron thickness, t_{ia} (mm)	16.0
Back iron thickness, t_b (mm)	5.6
Wire diameter, w_r (mm)	0.6
Number of winding/ slot (turns)	180
Resistance (one phase), R (Ω)	19.2 (at 20ºC)
Number of poles, N_p	8
Number of slots, N_s	16
Back iron material	S20C
PMs material	NdFeB – N40SH; $B_r = 1.26$T; $\mu_r = 1.05$

The other noticeable phenomenon is the different signs of the flux distribution on the coil phases. For example, it can be clearly seen from Fig. 4 that the flux distribution on coil 1 and coil 2 has a plus (+) sign, while the flux distribution on coil 3 and coil 4 has a minus (−) sign. Therefore, it is mandatory to prepare the setup to have a current direction exactly like the one in the FEM analysis, otherwise, the calculation of total power from each single phase will be subtracted and nearly zero [9].

The final design specifications of the tubular generator are summarized in Table 1 and the external circuit is shown in Fig. 5.

3. Analysis to Determine Validity

The instantaneous voltage of one coil centered at equilibrium position z_0 in the regenerative shock absorber is presented as a function of time, position, magnetic flux

density, geometrical parameters and the suspension velocity and frequency [10]:

$$V = B_0 L \cos\{\pi[z_0 - (v_{max}/\omega)\cos\omega t]/H\}v_{max}\sin\omega t \quad (7)$$

For the 0° coil, which has the maximum magnetic flux density, the voltage is calculated by:

$$V_{0°} = B_0 L \cos\left\{\frac{\pi v_{max}}{H\omega}\cos\omega t\right\}v_{max}\sin\omega t \quad (8)$$

If the vibration amplitude is small $v_{max}/\omega \ll H/\pi$, the regenerative voltage approximate a sine wave:

$$V_{0°} = B_0 L \left|\frac{j\omega}{\omega_n^2 - \omega^2 + 2j\zeta\omega_n\omega}e_{in}\right|\sin\omega t \quad (9)$$

and a 90° phase coil will have a double frequency wave:

$$V_{90°} = B_0 L \frac{\pi V_{max}^2}{2H\omega}\sin 2\omega t \quad (10)$$

Figure 6 presents the radial flux density across the middle of the coil at $t = 0.3$ s under the load condition. As mentioned above, when the load resistance on each phase is equal to the coil resistances, output power is maximum. For example, on phase 1:

$$R_{Load\,1} = R_{coil\,1} + R_{coil\,3} = 2 \times R_{coil\,1} = 2 \times R_{coil\,3} \quad (11)$$

Under a no-load condition, the voltage value of each phase is maximum, which is termed back EMF; while under a load condition, those voltage values are divided into two equal parts, load resistance and coil resistances, this is termed induced voltage. This means the value of the back EMF is double the induced voltage for the same phase.

Figure 7 shows the waveforms of the back EMF and the induced voltage, and confirms the expectation above. For instance, under a no-load condition, the maximum value of the back EMF of phase 1 is around 72.68 V, nearly two times that of induced voltage, which is approximately 36.27 V.
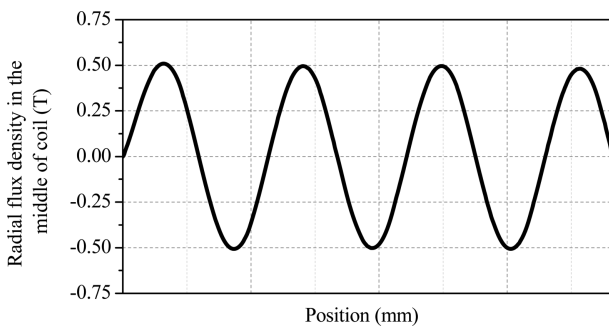
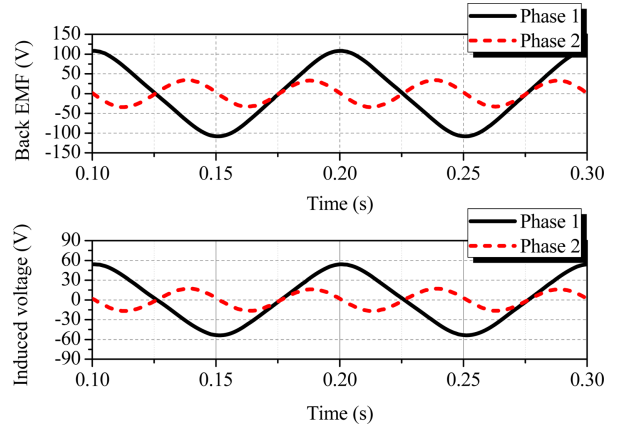In addition, the frequency of the voltage in phase 1 is

Fig. 7. (Color online) Back EMF and induced voltage.
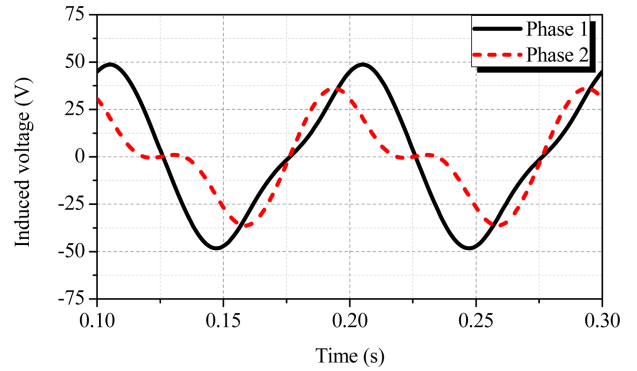

Fig. 8. (Color online) Induced voltage when the initial position is shifted by −5 mm.

10 Hz, while it is 20 Hz in phase 2. This phenomenon theoretically confirms the presented Eqs. (9) and (10).

Equation (7) indicates that, if the coils are not exactly in the 0°/180° or 90°/270° position, the regenerated voltage and current under excitation will not be in a sinusoidal waveform, even if the vibration amplitude is very small [10]. This induced voltage phenomenon is illustrated in Fig. 8, when the initial position is shifted by −5 mm. In
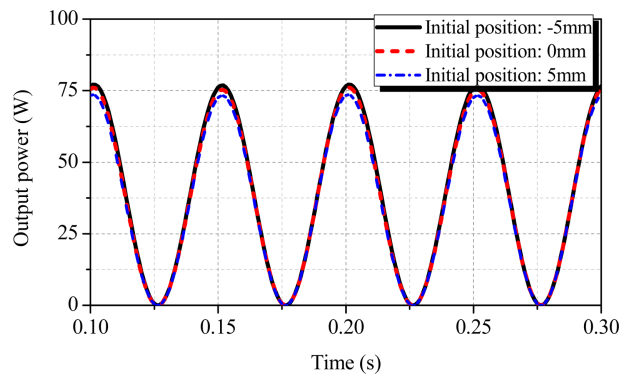

Fig. 6. Radial flux density across the middle of coil.

Fig. 9. (Color online) Output power for different initial positions.

Table 2. Analysis results for the proposed generator.

Item		Value
Vibration speed, v (m/s)		0.25
Vibration frequency, f (Hz)		11.25
Peak to peak stroke length (mm)		10.00
RMS Back EMF (V)	Phase 1	72.68
	Phase 2	23.68
RMS induced voltage (V)	Phase 1	36.27
	Phase 2	11.74
RMS current (A)	Phase 1	0.94
	Phase 2	0.31
Output power (W)	Maximum	76.09
	Average	37.78

this case, the value of the induced voltage on each phase is not half of its back EMF, the waveforms are distorted and the frequencies are also different.

Figure 9 compares the output power for different initial positions, including −5 mm, 0 mm, and 5 mm. Although the voltage and current are un-sinusoidal, the output power value and waveform are nearly similar.

The results of the analysis of the proposed generator are summarized in Table 2.

4. Experimental Verification of Analysis

4.1. Prototype and experimental setup

Based on the analysis, a prototype for experimental verification was fabricated as shown in Fig. 10. In order to protect the PM, a stainless steel sheet is wrapped around the surface of the PM layers. The coil windings are wound on a frame composed of Bobbin material, and inserted through a plate on the top to connect with a sub-motor.

Figure 11 shows the experimental setup: the main equipment includes a linear generator connected to a sub-motor through a gearbox, crank, and shaft; load resistors, power analyzer, and oscilloscope. The maximum speed of the sub-motor is 3000 rpm, and it is connected to a crank through a gearbox with a gear ratio of 5:1. Accordingly, the maximum rotating speed of the crank is 600 rpm.
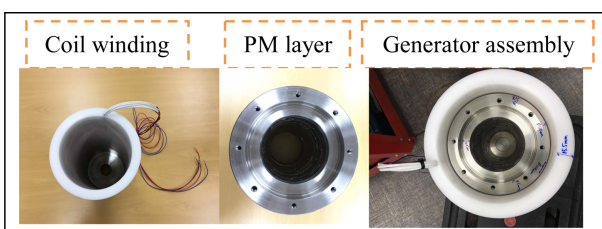
Fig. 10. (Color online) Prototype.
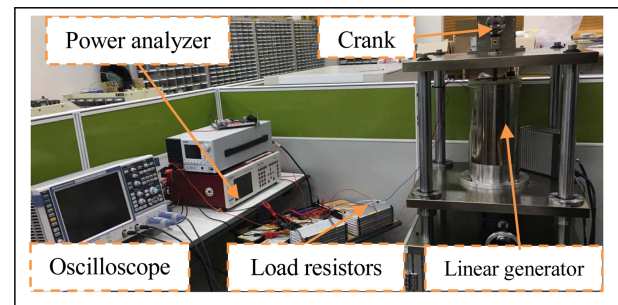
Fig. 11. (Color online) Experimental setup.

Table 3. Comparison of output power according to peak to peak stroke length.

Item	Stroke length$_{(p-p)}$ (mm)			
	7.5	11.25	35	40
Linear speed (m/s)		0.25		
Linear frequency(Hz)	15	10	3.22	2.81
Rotating speed on crank (rpm)	900	600	193.2	168.6
Rotating speed on sub-motor (rpm)	4500	3000	966	843
Maximum power (W)	−	76.1	76.8	75.7
Average power (W)	−	37.8	37.2	37.3

Under the reference conditions, the stroke length was 11.25 mm, vibrating speed was 0.25 m/s, so the rotating speed of the crank is equal to 600 rpm, which is the maximum operating speed. One solution to reduce vibrating speed is to use equivalent operating conditions by modifying the stroke length, for instance, 35 mm, while the vibrating speed remains at 0.25 m/s. In this case, the rotating speed of the crank is reduced to around 193.2 rpm. Although the voltage and current waveforms are distorted, the output power values are almost the same and the waveforms are still sinusoidal.

Impacts of the stroke length on output power were analyzed and the results are summarized in Table 3. Besides the reference peak to peak stroke length, the other considered values were 7.5 mm, 35 mm and 40 mm, which require the rotating speed of the sub-motor to be 4500 rpm, 966 rpm, and 843 rpm, respectively.

Finally, the third condition in Table 3, with 35 mm of stroke length, 0.25 m/s of linear speed and 3.22 Hz of linear frequency, was selected for verification with 2D FEA.

4.2. Effect of various vibrating speeds

Figures 12 and 13(a) show the value of the back EMF when the vibrating speed was 0.25 m/s and the stroke length was 35 mm. In that case, because of the the exact initial position, the frequency and waveform are well
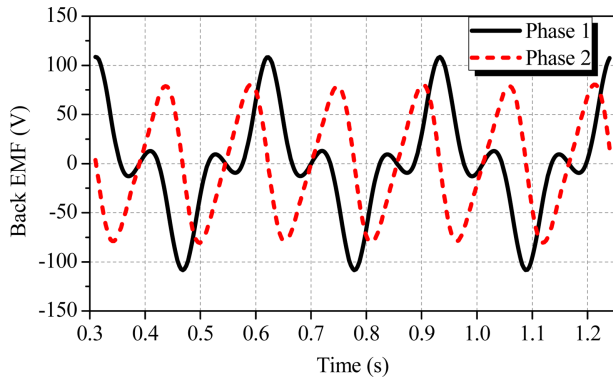
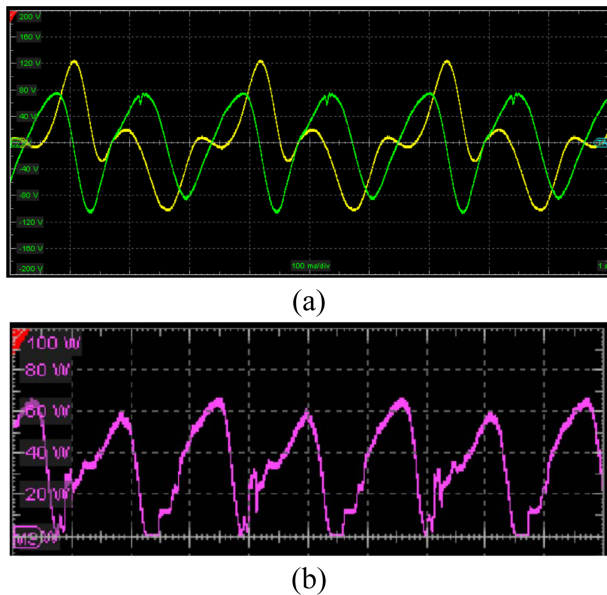**Fig. 12.** (Color online) Analyzed results showing the Back EMF.

(a)

(b)

Fig. 13. (Color online) Experimental results showing (a) Back EMF; (b) Output power under full load condition.

Fig. 14. (Color online) Comparison of the RMS induced voltage for different vibrating speeds.
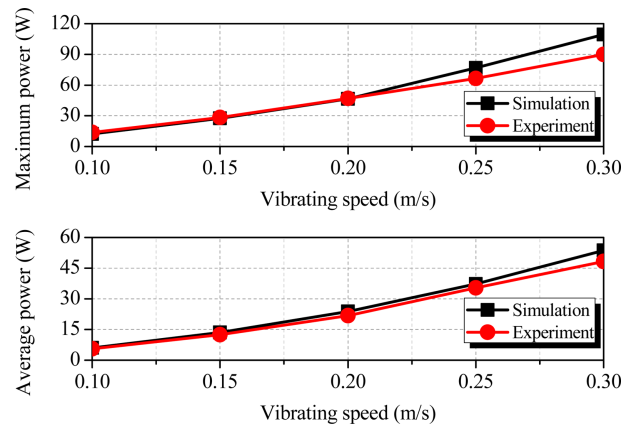
Fig. 15. (Color online) Comparison of the output power for different vibrating speeds.

matched with the analyses. The output power under the same speed and 100% load condition is shown in Fig. 13(b) and because of the experimental limitations, the full load resistance was fixed at 39 Ω instead of 38.4 Ω as it is in the calculation.

Figure 14 shows a comparison of the analytical and experimental results for the RMS induced voltage on each phase at several output linear speeds, or rotating speeds on the sub-motor, under 100% load resistance. The average difference between the RMS induced voltage was approximately 3.36%, and both the simulation and experiment results exhibited a similar trend.

The power variation for different vibrating speeds is presented in Fig. 15. It can be clearly seen that in the range from 0.1 m/s to 0.25 m/s, there is a good match
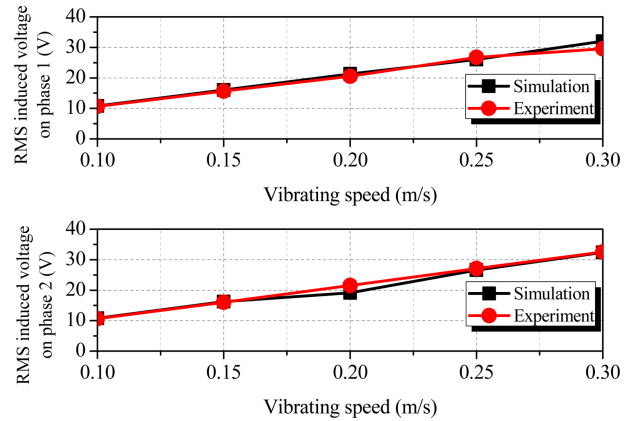
between simulation and experiment, however, when the vibrating speed is 0.3 m/s, the experimental results are excessive compared to the analyzed results.

This can be explained by the weakness of the experimental facilities, especially the crank and its corresponding bolts, which connect the sub-motor with the linear generator and transform rotating motion to linear motion. As a result, when the sub-motor is subjected to a high rotating speed, the body of the prototype and the crank experience significant shaking.

Overall, the average deviation in the average power and maximum power were about 7.32% and 9.23%, respectively.

A noticeable characteristic is the measured average power, which is exactly proportional to the square of the vibrating speed as expected in Eq. (3). For example, when the vibrating speed is 0.1 m/s, the measured average power before the drive is about 5.65 W. Accordingly, the average power under 0.15 m/s of vibrating speed can be
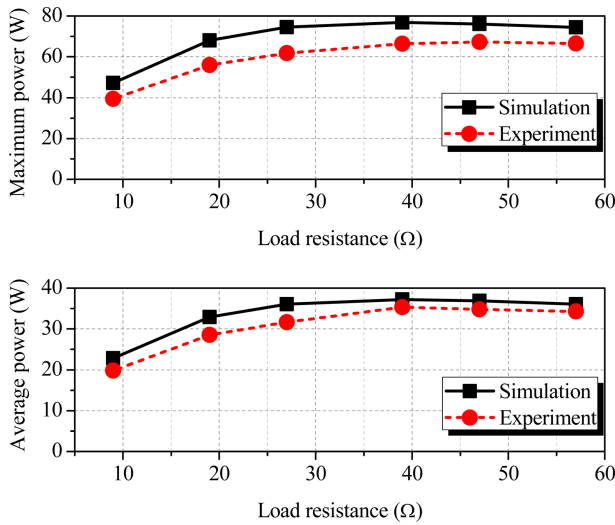
Fig. 16. (Color online) Comparison of the maximum output power for different load resistances.

expressed by:

$$P_{0.15\,m/s} = P_{0.10\,m/s} \times \left(\frac{0.15}{0.10}\right)^2 = 5.65 \times \left(\frac{0.15}{0.10}\right)^2 \approx 12.7\,(W)$$

This value agrees well with the measured average power from the experiment, which is nearly 12.5 W. The same phenomenon was also observed for the other vibrating speeds. When the vibrating speed was 0.25 m/s, the prototype can generate an average of 35.4 W, which is nearly 2.2 times higher than the model in [10].

4.3. Effect of various load resistances

The variation in measured output power for various load resistances was compared with simulation results, and is shown in Fig. 16. Because of the weakness of the experimental facilities, as mentioned in Section 4.2, the average deviation for maximum power and average power, 14.49% and 9.93%, respectively, are not really satisfactory.

However, in comparison with the previous designs in [10, 11], which exhibited an extreme difference between the analyzed and experimental results of over 50%, the average deviation shown for the proposed topology in this paper is a dramatic improvement.

In addition, the observation of a similar trend for load resistance values suggests that the analysis results are reliable.

4.4. Effect of various stroke lengths

The relation between three factors, peak to peak stroke length, vibrating frequency, and vibrating speed are expressed by Eq. (6):

Table 4. Experimental setup and expectations.

Stroke (mm)	Frequency (Hz)	Speed (m/s)	Average power (W)
22.50		0.10	5.51
11.25	2.0	0.05	1.32
7.50		0.033	0.67
11.25	4.0		5.10
7.50	6.0	0.10	4.60

$$Stroke = \frac{v_{rms}\sqrt{2}}{\pi f}$$

In this section, the generator is characterized for various stroke lengths and the performance results are confirmed with theoretical predictions, using in Eqs. (3) and (6). The corresponding experimental setup and results are listed in Table 4.

When the frequency is fixed at 2 Hz, if the stroke length is decreased two times from 22.5 mm to 11.25 mm, the average output power is reduced four times, from 5.51 W to 1.32 W, respectively.

In the other case, when the vibrating speed is 0.1 m/s, if the stroke length is increased by 1.5 times from 7.50 mm to 11.25 mm, the average power remains the same because of the inverse proportion between the stroke length and frequency.

All of the characteristics shown in Table 4 confirm there was good agreement between the theoretical analyses and experimental results.

4. Conclusion

This paper presented a design configuration, analyzed results and experimentally verified the performance of a single layered PM, a coreless tubular generator for energy harvesting in a suspension system in a sport utility vehicle. To verify the performance of the proposed machine, extensive 2D FEM was carried out using magnetic computations.

The validity of the analysis was carefully examined and confirmed by experiments, which showed acceptable agreement. It was also confirmed by experiment that an average output power of about 35.4 W can be generated when the vibrating speed is 0.25 m/s and the load resistance is fixed at 100%. The power behaviors of the proposed machine were also experimentally determined to be proportional to the square of the vibrating speed, and the average deviation was around 7.32%. The other characteristic of the proposed machine based on the changes in the load resistance, was also well matched with the analyzed data, with an average deviation of approximately 9.93%.

Given the general characteristics shown both analytically and experimentally, the proposed topology can be of interest for energy harvesting from the shock absorber of a sport utility vehicle. However, the main shortcomings are the big volume of the system, because of its large diameter, that leads to low power density.

Further study will focus on improving the output power, and reducing the size, which can result in improvements to the power density. Efficiency and thermal characteristics will also be considered.

Acknowledgments

References

[1] P. Li, L. Zuo, J. Lu, and L. Xu, Electromagnetic Regenerative Suspension System for Ground Vehicles, 2014 IEEE International Conference on Systems, Man, and Cybernetics, Oct. 5-8, 2014.

[2] Z. Li, L. Zuo, G. Luhrs, L. Lin, and Y. X. Qin, IEEE. Trans. Veh. Technol., **62**, 1065 (2013).

[3] Z. Li, Z. Brindak, and L. Zuo, Modeling of an electromagnetic energy harvester for vehicle suspensions, in Proc. ASME Int. Mech. Eng. Congr., Denver, CO (2011) pp. 285-293.

[4] X. Tang and L. Zuo, J. Intell. Mater. Syst. Struct., **23**, 2117 (2012).

[5] L. Zuo and P. Zhang, Energy Harvesting, ride comfort, and road handling of regenerative vehicle suspensions, in Proc. DSCC (2012) pp. 295-302.

[6] P. S. Zhang, Design of Electromagnetic Shock Absorber for Energy Harvesting from Vehicle Suspensions, Master of Science Thesis (2010).

[7] Y. Liu, Designs, Modeling and Control of Vibration Systems with Electromagnetic Energy Harvesters and their Application to Vehicle Suspensions, Doctor of Philosophy Thesis (2016).

[8] L. Zuo, X. Tang, and P. Zhang, Electricity-generating shock absorbers, U. S. Patent 31/368846, filed 07.2011.

[9] R. B. Goldner and P. Zerigian, Electromagnetic Linear Generator and Shock Absorber, United States Patent, Patent No: 6,952,060 B2, Date ofPaten, (2005).

[10] L. Zuo, B. Scully, J. Shestani, and Y. Zhou, Smart Mater. Struct., **19**, 045003-1-045003-10 (2010).

[11] X. Tang, T. Lin, and L. Zuo, IEEE/ASME Trans. Mecha., **19**, 615 (2014).

[12] M. T. Duong, Y. D. Chun, P. W. Han, B. G. Park, D. J. Bang, J. K. Lee, and H. Wook, Comparison Between Cored and Coreless Tubular Generator in Terms of Output Power and Output Power Density, 2017 KSAE Annual Spring Conference.

[13] B. L. J. Gysen, J. L. G. Jansen, J. J. H. Paulides, and E. A. Lomonova, IEEE Trans. Ind. Appl., **45**, 1589 (2009).